Technical Note

Landslides
DOI 10.1007/s10346-021-01762-x
Received: 12 May 2021
Accepted: 27 August 2021


Carolina Seguí · Manolis Veveakis

# Continuous assessment of landslides by measuring their basal temperature

**Abstract** In this study, we suggest a temperature-based assessment and mitigation approach for deep-seated landslides that allows to forecast the behavior of the slide and assess its stability. The suggested approach is validated through combined field monitoring and experimental testing of the El Forn landslide (Andorra), whose shear band material is Silurian shales. Thermal and rate controlled triaxial tests have shown that this material is thermal- and rate-sensitive, and in combination with the field data, they validate the theoretical assumption that by measuring the basal temperature of an active landslide, we can quantify and reduce the uncertainty of the model's parameters, and adequately monitor and forecast the response of the selected deep-seated landslide. The data and results of this letter show that the presented model can give threshold values that can be used as an early-warning assessment and mitigation tool.

**Keywords** Basal temperature · Landslide monitoring · Experimental tests · Constitutive equations · Numerical modeling

## Introduction

Deep-seated landslides typically involve a slow earth-motion over heavily deforming zones of intense shear (shear bands) at their base, before collapsing catastrophically (Lacroix et al. 2020). The shear bands are usually formed by clays or clay-like materials that can be very sensitive when the material is sheared and experiencing changes in pressure and temperature (Seguí et al. 2020). In earlier works, the authors (Veveakis et al. 2007; Seguí et al. 2020) presented a mathematical model that is able to reproduce the behavior of a deep-seated landslide from its secondary creep phase (Intrieri et al. 2019) to its catastrophic collapse (tertiary creep), considering the changes in temperature of the shear band material because of frictional heating (Goren and Aharonov 2007; Goren et al. 2010; Zhao et al. 2020). In this mathematical model, the constitutive equations used were following the work of Vardoulakis (2002), considering that the clay material located inside the shear band exhibits rate hardening (Leinenkugel 1976) and thermal softening (Hicher 1974), when the material is at a critical state (negligible volumetric changes when the material deforms). However, these theoretical considerations have never been tested in a controlled case of a deep-seated landslide with field data.

Previous experimental works on clay materials (Hueckel et al. 2009; Ferri et al. 2010) show that by increasing the temperature, their friction coefficient (i.e., the strength of the material) may decrease depending on the ability of the selected type of clay to absorb and expel water. Moreover, Blasio et al. (2017) presented a study on the effect of the frictional melting of a crystalline gouge of a landslide due to the increase in temperature when the sliding mass accelerates. On the other end, several authors have applied velocity stepping on experimental tests on clays and shales for shearing zones (e.g., Cappa et al. 2019; Bohloli et al. 2020), finding that the material's strength exhibits velocity hardening (i.e., stable slip on seismic faults). Additional studies of velocity stepping in salt rock for fault gouges show a dependency in the rate hardening and rate weakening depending on the range of velocity that is applied, as well as the particle size of the mineralogy (Rattez and Veveakis 2020) and its orientation (Niemeijer et al. 2010). However, the combination of rate and thermal dependence on a shear band material of an active landslide has never been tested before, as suggested here to be done for the active deep-seated landslide of the El Forn in Andorra (Seguí et al. 2020a).

On the field scale applicability of these concepts, we note that previous works show that landslides can be studied by remote sensing and ground-based radar interferometry (Corominas et al. 2014) as well as numerical modeling by hydro-mechanical coupling (Song et al. 2020; Lizárraga and Buscarnera 2020) to locate the areas of maximum deformation and sliding velocities. Once the critical parts of the landslide are located, the instrumentation of boreholes is performed to follow the groundwater pressure, being a triggering factor of acceleration of the landslide (Madritsch and Millen 2007; Lacroix et al. 2020; Agliardi et al. 2020; Bontemps et al. 2020), and the displacement by inclinometers or extensometers (Corominas et al. 2000). Gili et al. (2021) presented an extensive study on the complex Vallcebre landslide showing the different techniques applied to study the evolution of the movement. They applied surface techniques such as terrestrial photogrammetry and GPS among others, and borehole instrumentation, such as inclinometers, wire extensometers, and piezometers. They considered that by combining surface techniques with in-hole instrumentation the data can be validated with accuracy. However, there has not been any thermometer instrumented inside the shear band of a landslide to couple the possible thermal sensitivity of the material located in one of the most critical parts of a landslide.

In this letter, we show field data of an active lobe of the El Forn landslide (Seguí et al. 2020a), which includes the real-time, continuous monitoring of the temperature inside the shear band. Moreover, we test the material of the sliding zone of this lobe under thermal and velocity stepping, showing its response with varying loading velocity and temperature. Finally, we combine the field and experimental data with a mathematical model (Seguí et al. 2020) and constrain the model's parameters.

## Field monitoring and driving stresses of the El Forn landslide

The El Forn landslide is a large deep-seated landslide located in Andorra, in SW Europe. This landslide has a sliding mass of $\sim 300 Mm^3$ (Fig. 1a) that currently creeps with an average velocity of 0.5-2cm/year (Seguí et al. 2020a). Inside the landslide, the Cal Ponet–Cal Borronet lobe ($\sim 1 Mm^3$ of sliding mass) slides faster (Fig. 1a and b), with a velocity range of $1 - 4 cm/year$ (Corominas et al. 2014). This lobe (Fig. 1c) moves as a rigid block, as shown by the displacement data of Fig. 1e, over a deforming shear band (Fig. 1d), hence being the deep-seated landslide that our study will focus on. The lobe's shear band is located at 29m depth (Fig. 1e) and is formed by 80% Silurian shales very rich in phyllosilicates (muscovite, paragonite, and chlorite), and about 20% of quartz (Seguí et al. 2020a).

In the present study, we aim at validating the hypothesis that temperature is an important factor in the evolution and behavior of active deep-seated landslides (Vardoulakis 2002; Veveakis et al. 2007; Seguí et al. 2020). To this end, we present monitoring

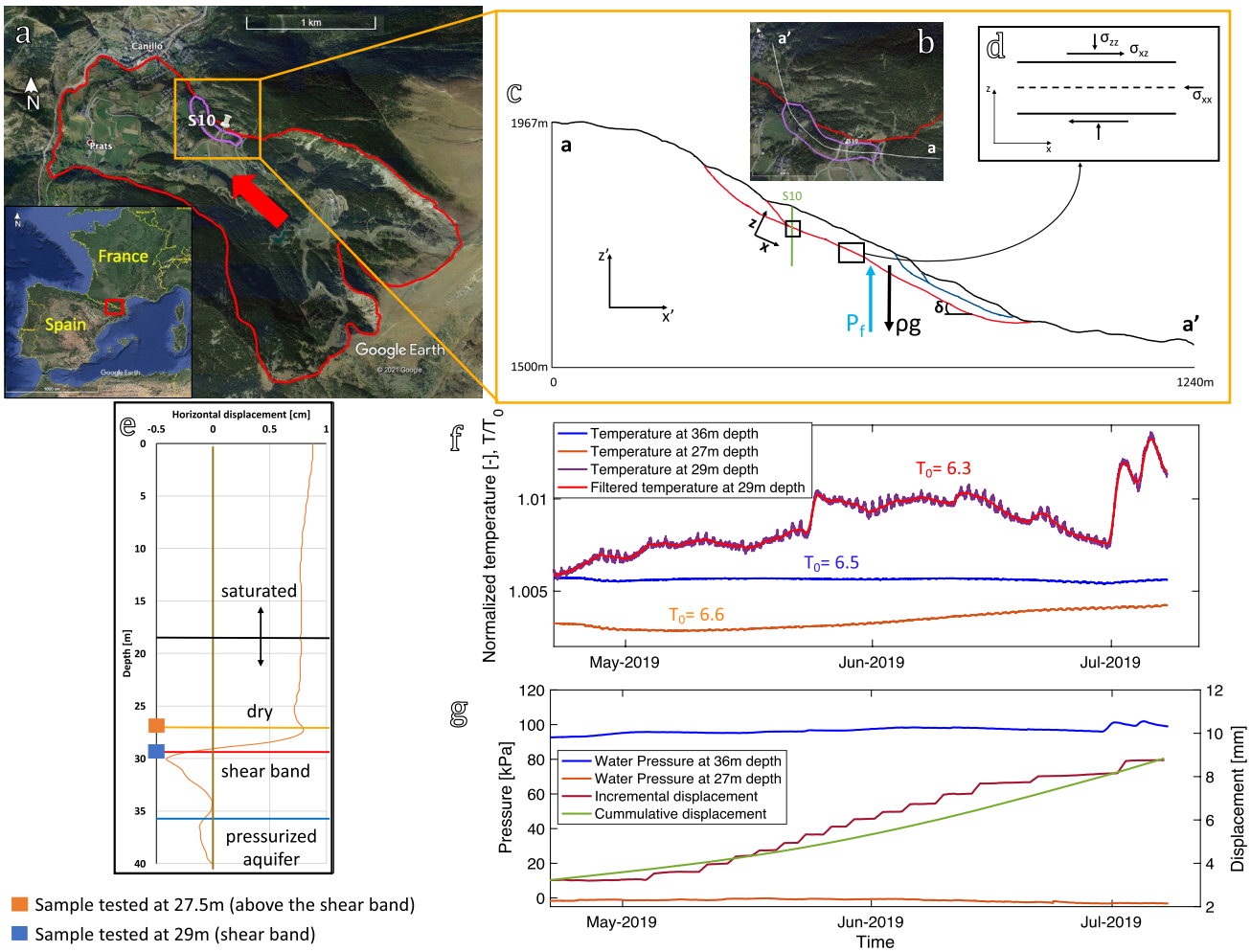


**Fig. 1** The deep-seated landslide of El Forn in Andorra. **a** Satellite image (©Google Earth) presenting El Forn landslide (in red), the red arrow indicating the direction of movement of the sliding mass, Cal Ponet–Cal Borronet lobe (in purple) with the location of the S10 borehole (white marker). The inset is a map of the SW Europe (©Google Earth) showing the location of Andorra Principality (highlighted in a red square). **b** Satellite image (©Google Earth) of a portion of the El Forn landslide (in red), and the Cal Ponet–Cal Borronet lobe (in purple) with the white line a-a' of the profile for Fig. 1c. **c** Profile of the Cal Ponet–Cal Borronet lobe across the a-a' line (Fig. 1b). The sliding surface (in red) with the main forces acting on the shear band (blue and black arrows). **d** Model of the shear band of the landslide, with the main forces acting on the layer. **e** Data and sensors in the S10 borehole. Data of the displacement-vs-depth of the inclinometer, from April to June 2017 (EuroconsultSA 2017). The lines indicate the following: the horizontal red line for the location of the thermometer, the horizontal blue line for the location of the piezometer at 36m depth, the orange line for the location of the piezometer at 27*m* depth, the horizontal black line the piezometer at 18*m* depth, and the brown vertical line for the extensometer. The two squares represent the depth of the samples tested in the experimental part of the study. **f** Normalized (with respect to their background value listed on each curve) field temperature data from the end of April until July 8th of 2019. Temperature readings of the thermometer (29*m* depth) and the two piezometers (27 and 36*m* depth) were installed in the S10 borehole. The graph shows the raw data of readings every 20 minutes, and the daily average only for the thermometer. **g** Water pressure data of the piezometers (27 and 36*m* depth), and the incremental and cumulative displacements of the lobe. The graph shows the raw data with readings every 20 minutes

results from the Cal Ponet–Cal Borronet lobe. The instrumentation installed in this lobe is inside the S10 borehole (Fig. 1b) and consists of an extensometer (measuring the horizontal displacement), two piezometers (measuring the water pressure) located at $27m$ depth and at $36m$ depth (i.e., one above and one below the shear band), and a thermometer installed inside the shear band (with a resolution of $0.1°milliC$) at $29m$ depth (Fig. 1e). The piezometers also measure the temperature of the water, which allows to compare temperatures with the one from the thermometer at the shear band. In Fig. 1f, the three temperatures are depicted, with the temperatures above and below the shear band being constant and higher than the one at the shear band. The latter presents variations which follow exactly the same trend as the water pressure below the shear band (Fig. 1g). The piezometer above the shear band (Fig. 1g) does not have any pressure reading, which indicates that the shear band could be acting as an impermeable barrier that forms an artesian (confined) lower aquifer under elevated pressure. Despite the small variations of temperature inside the shear band (between 6.34 and $6.39°C$), it is clear that the variations are significantly higher than the instrument's resolution and the temperature evolution is linked to the pressurized aquifer below and the displacement of the landslide. What is not clear, however, is the interplay and sequence between these three fields. Is the pore-pressure increase in the aquifer triggering the motion, which in turn raises the shear band temperature? Or it is the increased temperature of the pressurized water causing the shear band temperature to increase, and the slope to move? Answering these questions by identifying the dominant mechanisms operating at depth, is the goal of the present work.

To do so, we begin by highlighting that the difference in temperature of the shear band with the temperature of the piezometers could indicate that the shear band is isolated from groundwater flow across it, as the shear band has the lowest temperature and its material is impermeable. Figure 1g also shows the displacement of the lobe, presented both as the raw (incremental) displacement received by the extensometer and as the overall cumulative displacement (distance) of the slope. As shown in Fig. 1f and g, the temperature signal is very sensitive to changes in pressure of the lower aquifer, essentially echoing any pressure variations within a day and preceding displacement variations by approximately two days. It therefore seems that, despite having negligible absolute reading, variations of the thermometer can be used as a precursor of the deformation variations. To assess whether this is indeed the case, or these variations are merely related to the landslide's motion, appropriate models need to be used, incorporating the field data and the response of the shear band.

With the field data presented in Fig. 1, we can interpret that the landslide is sensitive to pressure variations of the lower aquifer, which varies due to the snow melting and seasonal precipitation from the top of the mountain. Since the aquifer is under pressure, therefore driving the sliding process, the applied driving shear stress $\tau_d$ on the sliding interface at a depth $D$ normal to the surface, dipping at an angle $\delta = 30°$ can be calculated as: $\tau_d = \rho g D \sin(\delta)$, where $D = H\cos(\delta)$ ($H$ being the depth along the gravity axis), and $\rho$ is the total density experienced by the sliding surface. This is including the density of the overburden (density of the dry soil, saturated soil, and of the water) plus the specific gravity of the water of the pressurized lower aquifer (see Fig. 1). Under these considerations, the driving shear stress on the sliding surface is $\tau_d = (\sigma'_n + p_f)\cos(\delta)\sin(\delta)$ (where $\sigma'_n$ is the normal effective stress of the overburden acting on the sliding surface, and $p_f$ the pore fluid pressure of the pressurized aquifer acting opposite to the normal convention of Terzaghi's effective stress), or equivalently

$$\tau_d = \tau_{d,ref}\left(1 + \frac{p_f}{\sigma'_n}\right),\ \tau_{d,ref} = \sigma'_n \cos(\delta)\sin(\delta) \tag{1}$$

The overburden is featuring $29.5m$ of rock, part of which (the top $18 - 25m$) is admitting pore fluid due to seasonal precipitation, forming a perched (unconfined) seasonal aquifer at the top of the topography that does not contribute to the water table. Because of seasonal variations in the regional precipitation, this perched aquifer can vary significantly (it is estimated to be between $10 - 25m$ at any given point), thereby forcing the normal effective stress, $\sigma'_n$, at $29.5m$ depth to vary between $650 - 820kPa$. This, in turn, is restricting the driving reference shear stress, $\tau_{d,ref}$, on the sliding surface to be between $250 - 350kPa$.

## Experimental tests and mathematical model

### Rate and thermal sensitivity of the shear band material

To understand the behavior of the shear band's material and assess the physical processes behind the response of the shear band, we have performed experimental tests on this material (Fig. 1e) in a thermal triaxial machine with velocity and temperature control. The response of the material under shearing depends on parameters such as thermal diffusivity, rate sensitivity, thermal sensitivity, as well as the thickness of the shear band (Vardoulakis 2002; Veveakis et al. 2007; Seguí et al. 2020). Two of the aforementioned parameters, thermal and rate sensitivities, can be obtained in the laboratory (Hicher 1974; Leinenkugel 1976; Hueckel et al. 2009). The experimental tests presented in Fig. 2 have been performed on remolded core samples from the shear band of the Cal Ponet–Cal Borronet lobe, located between 29 and $29.5m$ depth (Fig. 1e). These samples are Silurian shales (Clariana et al. 2004) and have been previously characterized mineralogically (Seguí et al. 2020a), showing that the fabric of the samples of the shear band is completely aligned and parallel to the shearing direction.

For the tests performed on all the samples in the triaxial machine, we have followed the following protocol: as the cylindrical samples ($38mm$ diameter, $65mm$ height) are not consolidated after being remolded at the reported field humidity, we have first performed a triaxial compression on the samples at varying pressures between $200 - 900kPa$ in undrained conditions to calculate a friction angle of 30° at critical state and a negligible cohesion of $10kPa$. Next, we have performed thermal and rate sensitivity tests at critical state: at $200kPa$ confinement, we have increased the axial load at a constant rate, with loading–unloading cycles to eliminate any inertia effects stemming from the frame's rigidity, until the sample reaches a critical state at which the deviatoric (differential) stress ($q$), confining stress, volume, pore pressure, and temperature remain constant (Fig. 2a).

While at critical state, velocity stepping is performed (Fig. 2b) at 5 different velocities (from $0.0001 - 1mm/min$), allowing the sample to relax to a new critical state before performing the next velocity step. Through this exercise, the rate sensitivity of the material's shearing resistance at critical state, $q_{cs}$, is evaluated (Fig. 2c). Once

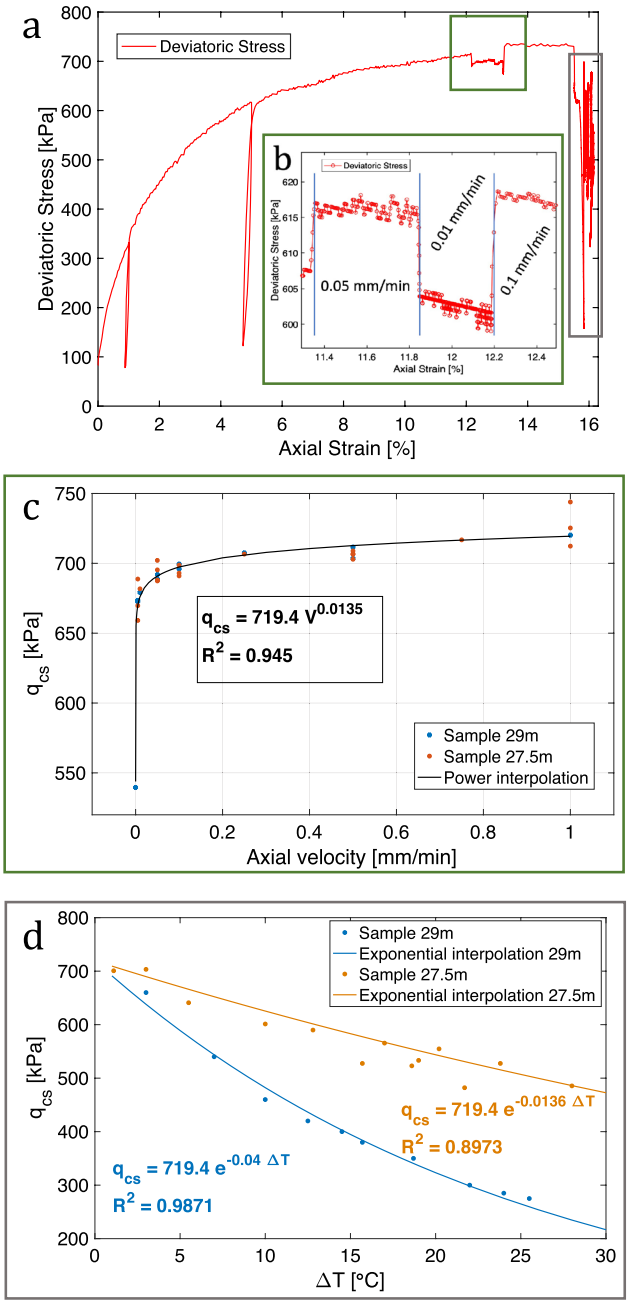


**Fig. 2** Experimental results. **a** Graph of axial strain [%] and deviatoric stress, $q$ [$kPa$], showing the evolution of the axial load in triaxial compression with three axial load-unload cycles, velocity steps, and increase in temperature. **b** Graph of axial strain [%] and deviatoric stress,$q$ [$kPa$], showing different axial loading rates. **c** Graph of axial velocity [$mm/min$] with deviatoric stress at a critical state, $q_{cs}$[$kPa$], showing the data obtained in the experiments (dots) for the materials outside and inside the shear band, and the fitting as a power interpolation (line) of the two materials, being the same for both materials, suggesting that the rate dependence is sensitive to the samples' mineralogy. The power interpolation fitting allows obtaining the rate sensitivity law for this material by showing that the material is rate hardening for both depths. **d** Graph of the increment of temperature [°$C$] in the sample ($\Delta T = T - T_{ref,lab}$, being $T_{ref,lab} = 20°C$), with deviatoric stress at critical state, $q_{cs}$ [$kPa$], showing the data obtained in the experiments (dots) and the fitting as an exponential interpolation (lines), for each material. The exponential interpolations indicate that both materials are thermal softening, with higher sensitivity exhibited by the one inside the shear band, a response strongly linked to the fabric orientation of the minerals

the velocity steps are completed, the sample is kept at critical-state by holding its volume and allowing it to relax to the slowest critical state possible by the machine's specifications, at $V = 10^{-9} mm/min$ (Fig. 2a). At this point, the thermal tests start by keeping the confining pressure and loading velocity constant, and only increasing the temperature of the sample to obtain the thermal sensitivity of the material (Fig. 2d). For the thermal tests, we have increased the temperature slowly at steps of $2 - 3°C$, inducing a rate of $1.5°C$ per hour before letting it equilibrate to a new critical state for a couple of hours. The temperature of the sample was monitored with a thermal probe less than $10mm$ away from the sample, and temperature was held constant until this probe stabilized to a steady state. Once the temperature of the sample and the axial stress are equilibrated, at each temperature variation, we mark the deviatoric stress values to obtain the thermal sensitivity of the material shown in Fig. 2d.

Following the rate and thermal sensitivities tests, we may now combine the two effects on the shearing resistance of the material (Fig. 2c and 2d), by accepting the multiplicative decomposition suggested by Vardoulakis (2002):

$$q_{cs} = f(\dot{\gamma})g(T) = q_{ref}\left(\frac{\dot{\gamma}}{\dot{\gamma}_{ref}}\right)^{N} \exp\left(-M\Delta T\right) \tag{2}$$

where $\dot{\gamma} \approx V/H$ is the deviatoric (differential) strain rate calculated in the laboratory under negligible radial deformation rate ($H$ being the height of the sample, in this case $65mm$). From the experimental results of the El Forn shear band material, we obtain $M = 0.04°C^{-1}$, $N = 0.0136$, $q_{ref} = 719.4kPa$ and loading rate $\dot{\gamma}_{ref} = V_0/H = 2 \times 10^{-4}\, s^{-1}$ (being $V_0 = 1mm/min$). Eq. (2) can be solved for the strain rate, $\dot{\gamma}$, to obtain the following visco-plastic flow law formulated for clay and clay-like materials, as follows:

$$\dot{\gamma} = \frac{\partial V}{\partial z} = \dot{\gamma}_{ref}\left(\frac{q_{cs}}{q_{ref}}\right)^{1/N} e^{m\Delta T},\ m = \frac{M}{N} \tag{3}$$

It is worth noticing that we have performed the same tests for the samples located outside the shear band, to compare the values of thermal and rate sensitivity (Fig. 2c and d). We find that the samples have the same rate sensitivity coefficient $N$, but different thermal sensitivity coefficients $M$, with the material outside the shear band being less sensitive to thermal variations. All these samples are Silurian shales (Clariana et al. 2004) and have been previously characterized mineralogically (Seguí et al. 2020a), showing that they have the same mineral composition but different fabric orientation. In particular, the fabric of the samples of the shear band is completely aligned and parallel to the shearing direction, but outside this area, the fabric is randomly oriented. It, therefore, seems that the mineralogy of the material drives its rate sensitivity, whereas thermal sensitivity is predominantly controlled by their fabric (orientation of the mineralogy).

## Mathematical model of a deep-seated creeping landslide

The mathematical model and the constitutive equations used to forecast the behavior of a deep-seated landslide were first described by Vardoulakis (2002) and then implemented by Veveakis et al. (2007) and Seguí et al. (2020) for the Vaiont

landslide (Italy) and the Shuping landslide (in Three Gorges Dam, China). The equations used in the mathematical model focus on the behavior of the material located inside the shear band and assume that the material is at critical state (deforming under constant volume), fully saturated in water, visco-plastic, and its mechanical properties vary along the vertical axis, $z$, of the shear band (Fig. 1d).

Using the arguments presented in details by Rice (2006), Veveakis et al. (2007), and Seguí et al. (2020), stress equilibrium inside the shear band ($\frac{\partial \sigma'_{xz}}{\partial z} = \frac{\partial \sigma'_{zz}}{\partial z} = 0$) yields constant profiles of the effective stresses inside the shear band and equal to their external values: $\sigma'_{xz} = \tau_d(t)$ for the shear stress, and $\sigma'_{zz} = \sigma'_n(t)$ for the normal stress. Correspondingly, since the material is at critical state (i.e., deforming under constant volume), the mass balance yields the incompressibility condition for zero volumetric strain rate $\dot{\epsilon}_V = \dot{\epsilon}_{zz} = 0$. Therefore, the main equation describing the response of the basal material is the energy equation (Vardoulakis 2002; Rice 2006; Veveakis et al. 2007; Seguí et al. 2020), reading:

$$\frac{\partial T}{\partial t} = c_{th}\frac{\partial^2 T}{\partial z^2} + \frac{\sigma'_{xz}\dot{\epsilon}_{xz}}{\rho C_m} \tag{4}$$

with boundary conditions $T = T_{boundary}$ at the boundaries of the shear band, $z = -\frac{ds}{2}, \frac{ds}{2}$ ($ds$ is the thickness of the shear band). In this equation, $\rho C_m$ is the heat capacity of the shear band material, $c_{th} = jk_m/\rho C_m$ is the thermal diffusivity, and $jk_m$ being the thermal conductivity.

To fully characterize the dependence of the shear stress, $\tau_d$, on the groundwater pressure and its variations, a regional hydro-geomechanical model is required, as described by Seguí et al. (2020). In the specific case under consideration, the El Forn landslide, such an analysis cannot be easily performed since the landslide is fed/loaded from the pressure changes of the groundwater below the shear band, as mentioned previously. These changes are not communicated to the overburden, since as discussed in Section 2 the shear band is acting as a flow barrier. This, in turn, suggests that water pressure variations below the shear-band directly affect the loading of the landslide following Eq. (1).

Following all these considerations, and recalling that in a 1D direct shear setting the differential stresses in Eq. (1) can be converted to shear stresses through $q = \sqrt{3}\tau_d$, Eqs. (3), (4) and (1) can be combined and further be reduced to a single parameter dimensionless equation

$$\frac{\partial \theta^*}{\partial t^*} = \frac{\partial^2 \theta^*}{\partial z^{*2}} + Gr\, e^{\theta^*},\ z^* \epsilon [-1, 1],\ t > 0 \tag{5}$$

where the following dimensionless parameters have been used:

$$z^* = \frac{z}{\left(\frac{ds}{2}\right)},\ t^* = \frac{c_{th}}{\left(\frac{ds}{2}\right)^2} t,\ \theta^* = m\left(T - T_{boundary}\right) \tag{6}$$

The dimensionless group, $Gr$, is the so-called Gruntfest number, Gruntfest (1963), defined as follows:

$$Gr = G_0\left(1 + \frac{p_f}{p_{f0}}\right)^{1+1/N} \tag{7}$$

with

$$G_0 = m\frac{\dot{\gamma}_{ref}}{jk_m}\frac{ds^2}{4}\tau_{d,ref} \tag{8}$$

The Gruntfest number (Gruntfest 1963), $Gr$, expresses the ratio of the mechanical work converted into heat over the heat diffusion capabilities of the material. This parameter includes all the material properties at hand (thermal conductivity, rate and thermal sensitivities, and reference rate), as well as the thickness of the shear band, $ds$, and the shear stress, $\tau_d$, applied on the shear band from the external loading sources (gravity and groundwater). Following the considerations thus far, $Gr$ evolves with the groundwater pressure, $p_f$, and therefore, with time, acts as a link between the external loading conditions with the internal response of the material. Since this is the only parameter of the mathematical equations, the performance of the model depends on accurately constraining the value of $Gr$. To constrain the value of $Gr$, we need to calculate the reference shear stress, $\tau_{d,ref}$, in the field and the thickness of the shear band, $ds$, from the parameters obtained in the laboratory (meso-scale) and the data from the field (field-scale). Therefore, the upscale strategy that we implement is to consider the values of $M$ and $N$ from the experiments as constant, and the rest of the parameters needed are environmental; hence, we will use the field parameters and knowing that the slope of the slide (shown in Fig. 1c) is approximately 30°, which is the same as the static friction angle of the material. Note that when thermal sensitivity is not considered ($M = 0$), the equations are amended as presented in Appendix A.

## Results and discussion

Following Eqs. (5-8), we assume the values of $N$ and $M$ from the experiments, an ambient temperature for the shear band at the field of $T_{boundary} = 6°C$, the pore pressure, $p_f$, being the water pressure from the piezometer at 36m depth, and $p_{f0} = 102kPa$ being the maximum value of water pressure in history from the same piezometer. With these as input, we use the readings of the shear-band temperature to calculate the optimal value of the reference Gruntfest number, $G_0$. To do so, we have used a Monte Carlo sampling approach (Hastings 1970; Raychaudhuri 2008), by sampling 500 random points in the log-normal distribution of $G_0$, shown in the inset of Fig. 3a. Following this sampling, Eq. (5) was solved 500 times, and the solutions have been compared with he field temperature, as shown in Fig. 3a. By calculating the least square error of the Monte Carlo simulations with the field temperature, we then obtained the simulation with the least error (Fig. 3a). This solution allowed us to obtain the value of $G_0$ that minimizes the error and fits the field temperature best, $G_0 = 4.5 \times 10^{-5}$ [−] (Fig. 3a) when $M \neq 0$ (red line). In case where the material is considered thermally insensitive (i.e., $M = 0$), then an equally good fit is obtained, with the reference value of the Gruntfest number (see Appendix A, Eq. 12) being $G_{M0} = 6 \times 10^{-5}$[−] (see Fig. 3b).

Once the temperature is calculated, the next step is to determine the velocity, $V$, and cumulative displacement, $u$, of the landslide. This is achieved in our model by integrating in time and space the strain rate (Eq. 3). For the velocity:

$$V = \int_{-ds/2}^{ds/2} \dot{\gamma} dz = V_0 \int_0^1 \left(\frac{p_f}{p_{f0}}\right)^{1/N} e^{\theta^*} dz^* \tag{9}$$

The reference (initial) velocity of the field can be calculated from the displacement data to be approximately $V_0 \sim 1cm/year$, a value

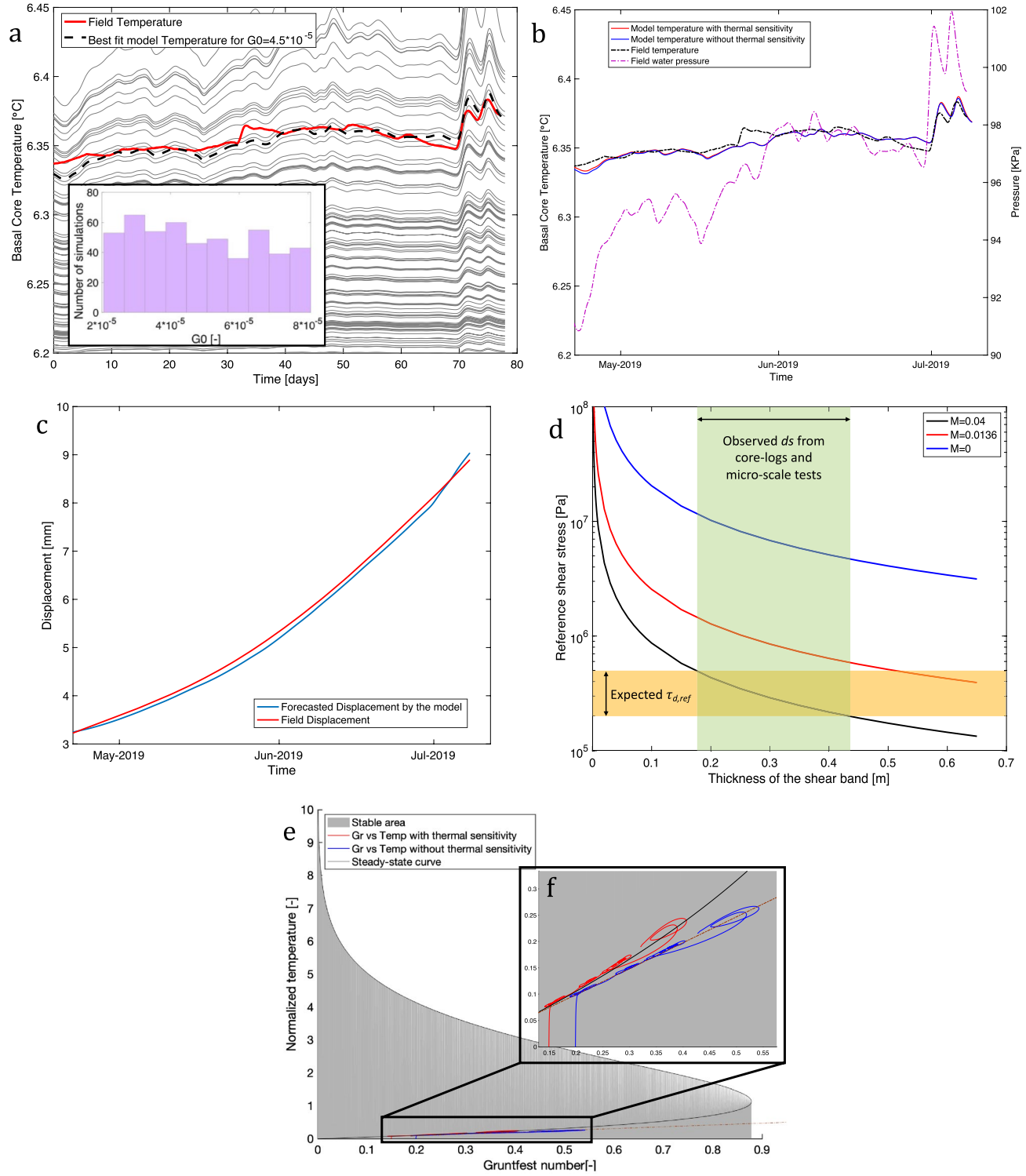


that is in accordance with the literature values as well (Corominas et al. 2014). Upon numerical time integration of the velocity of the model, Eq. (9), the model forecasts satisfactorily the landslide's displacement, as shown in Fig. 3c, producing the same curve for the cumulative displacement for any value of thermal sensitivity $M$ (including no thermal sensitivity, $M = 0$) assumed in Fig. 3b. This result raises the question, whether considering thermal sensitivity of the material is required, given the low values of temperature variations reported by the thermometer.

To answer this question, we will proceed with inverting the values of the real parameters included in the expressions of the reference Gruntfest numbers for each case, Eqs. (8, 12). To do so, we start by recalling that the shear band material consists of phyllosilicates (Seguí et al. 2020a), and we therefore accept the standard

◂**Fig. 3** Results of the mathematical model. **a** Graph of the shear-band temperature [$°C$] over time [*days*]. The gray lines show samples from the 500 simulations of Monte-Carlo of the temperature calculated at different values of $G_0$. The black dashed line is the best fit of the calculated temperature with the field temperature, for a value of $G_0 = 4.5 \times 10^{-5}$ with a thermal sensitivity of $M = 0.04$. **b** Graph of the shear-band temperature over time. The black dashed line is the best fit of the calculated temperature with the field temperature, for a value of $G_0 = 4.5 \times 10^{-5}$ with a thermal sensitivity of $M = 0.04$. The same fit of the calculated temperature has been obtained for the case without thermal sensitivity, $M = 0$ with a value of $G_{M0} = 6 \times 10^{-5}$ (see Eq. 12). The graph also shows the field water pressure from the piezometer at 36*m* depth over time. **c** Graph of displacement [*mm*] over time [*days*]. The blue line is the forecasted calculated displacement in the model, and the red line is the field displacement. **d** Inversion of the reference shear stress, $\tau_{d,ref}$, with the thickness of the shear band, $d_s$. The three curves have been calculated with Eq. (8), for different thermal sensitivities. The shaded areas of the graph indicate the most probable values of the field: thickness of the shear band in green, and reference shear stress in yellow. **e, f** Stability of the Cal Ponet–Cal Borronet landslide, showing the evolution of the Gruntfest number with the temperature, calculated with Eq. (5). The red line is the temperature-Gr solution of the model (shown in Fig. 3a as time series) calculated for a thermal sensitivity of $M = 0.04$, and the blue line is the same for no thermal sensitivity ($M = 0$)

literature values (Vardoulakis 2002) for their thermal conductivity $jk_m = 0.45\, J/°Cms$, and thermal diffusivity $c_{th} = 1.6 \times 10^{-7} m^2/s$. Note that these values have small deviations across all clay materials (Ghuman and Lal 1985) and are hereby considered to have no uncertainty. Having constrained these values, the remaining parameters in the expression of *Gr* are the reference values of the loading stress, $\tau_{d,ref}$, and the shear band thickness, $d_s$. Both quantities cannot be easily determined from field data of a single borehole, mainly because of the lack of representativeness of the values in the field scale. As discussed by Seguí et al. (2020a), visual investigations of the material retrieved from the borehole S10 of the field (see Fig. 1c) suggest that the shear-band thickness, $d_s$, should be between a few centimeters, up to half a meter thick. However, this is information received from a single borehole and cannot be constrained or validated further. Correspondingly, and as discussed in Section 2, the reference shear stress, $\tau_{d,ref}$, acting on the shear band may vary between $250 - 350kPa$.

With these values as input, and considering the best-fit values of the reference Gruntfest numbers, we use Eqs. (8, 12) to invert for the shear band thickness, $d_s$, and the driving background stress, $\tau_{d,ref}$. In Fig. 3d, we have plotted the inverted $\tau_{d,ref} - d_s$ space that provides the fits of Fig. 3b and 3c, using three different values of the thermal sensitivity, *M*. The plot shows that by removing the thermal sensitivity (i.e., setting $M = 0$ in Eq. 2), the reference shear stress from the field is inverted to be between 6 and $15MPa$. This range of reference shear stress in the field is not possible at the shallow depth that the shear band is located, therefore highlighting the necessity to consider the thermal sensitivity of the material. Indeed, when the thermal sensitivity derived in our experimental campaign is assumed, $M = 0.04$, the inverted values are in agreement with the expected ones in the field. To highlight further the importance of considering thermal sensitivity, in Fig. 3d we have added the results of considering the material outside the shear band (Fig. 1e) as the dominant material driving the process. In that sense, we have set $M = 0.0136$, and see that the reference shear stress for the range of thickness of the shear band is still higher than acceptable at that depth (between 60 and $180kPa$ for the $30m$ depth). Nonetheless, we observe that even this small value has an important effect in providing a more realistic explanation of the response of the landslide, suggesting that the thermal sensitivity of the material cannot be ignored.

In addition to reconciling the observations, the inclusion of thermal sensitivity in the material's response has important implications on the response of the mathematical model and the information it can offer. By performing a simple bifurcation analysis on the mathematical model of Eqs. (5,10) (see Seguí et al. (2020), for details), and by plotting the solution of the model in its $Temperature - Gr$ phase space, we can see in Fig. 3e and 3f that for $M = 0$ the temperature and the Gruntfest number follow an unconditionally stable branch of the phase-space (Veveakis et al. 2010), which indicates that the lack of thermal sensitivity suggests that the landslide will never collapse. On the contrary, for $M \neq 0$, the *Gr* and *Temperature* vary along the lower branch of a conditionally stable curve, thus suggesting that the system can become unstable past a critical value of $Gr - \theta^*$, and therefore, the landslide could collapse. From these results, we conclude that if the material is thermally insensitive, the model forecasts that the landslide will be unconditionally stable and will always be creeping in a stable manner. However, even the smallest amount of thermal sensitivity will cause the mathematical response of the model to offer an area of instability, whereby the landslide could transition from stable to tertiary creep and catastrophic collapse. This difference can be of critical importance for decision making, since operational protocols for unconditionally stable settings differ considerably than those that have the viable potential of admitting catastrophic collapse.

## Conclusions

This letter has presented the field and experimental data of the Cal Ponet–Cal Borronet lobe inside the large El Forn landslide (Andorra). This lobe is a deep-seated landslide as the field data show in Fig. 1. The novelty of this letter is that we have instrumented the slide with a thermometer inside its shear band to validate the assumption that the landslide should be assessed by considering the thermal evolution of the sliding mass to offer forecasting and controlling capabilities. The field data show that indeed the temperature of the shear band of the lobe is affected by the pressurized aquifer below, and by an increase in first the pore pressure and temperature, the slide accelerates. Moreover, we have presented the experimental results on the material of the shear band of this lobe. The velocity stepping and thermal tests have shown that indeed the material is thermal and rate sensitive. The results have shown that these Silurian shales are rate hardening and thermal softening, proving thus the theoretical assumption postulated by Vardoulakis (2002).

The mathematical model used to forecast the behavior of the lobe (i.e., displacement) has as input values the field and experimental data combined, and has been previously tested for two landslides: the Vaiont landslide that collapsed, and the Shuping landslide that remains active (Seguí et al. 2020). This numerical model (Veveakis et al. 2007; Seguí et al. 2020) assumes that there

is a thermal response of the shear band's material that affects the behavior of the slide, which has been demonstrated by the field and experimental data. As there is field and laboratory data available, the model has been almost fully constrained and we have only needed to invert for two unknown parameters: the reference shear stress of the field and the thickness of the shear band. The inversion of these values can be relatively easy to perform as the reference shear stress can be calculated within a range by knowing the depth, groundwater information, and specific unit weight of the overburden material. The thickness of the shear band can be constrained within a range from the micro-structure studies and field data. As the uncertainty of the model could be reduced by adding data from additional boreholes and modeling more sections of the slide, this study has shown a first step of validating and proving that thermal sensitivity plays a critical role in the stability of the landslide. It is therefore expected that, by monitoring the basal temperature of the landslide and fully characterize the material of the shear band (at micro and meso-scale), the suggested approach can be constrained and give both, forecasting and stability assessment capabilities.

## Acknowledgements

The authors would like to acknowledge Xavier Planas from the Government of Andorra to provide us the core samples of the landslide and the field data and Jose Moya from BarcelonaTech University to provide us the field data. Support by the NSF CMMI-2006150 project is also acknowledged. All the data used in this study are openly available at https://eartharxiv.org/repository/dashboard/1730/.

## Funding

Open Access funding enabled and organized by Projekt DEAL.

### Declarations

**Conflict of interest** The authors declare that they have no conflict of interest.



## A Equations for zero thermal sensitivity

Note that, in case there is no thermal sensitivity in the material, then $M = 0$ and the normalized final equation reads:

$$\frac{\partial \theta^*}{\partial t^*} = \frac{\partial^2 \theta^*}{\partial z^{*2}} + Gr\,,\ z^* \epsilon [-1, 1],\ t > 0 \tag{10}$$

where the dimensionless temperature now reads $\theta^* = (T - T_{boundary})/T_{boundary}$. The Gruntfest number (Gruntfest (1963)), $Gr$, becomes in turn:

$$Gr = G_{M0}\left(1 + \frac{p_f}{p_{f0}}\right)^{1+1/N} \tag{11}$$

with

$$G_{M0} = \frac{\dot{\gamma}_{ref}}{j k_m T_{boundary}} \frac{ds^2}{4} \tau_{d,ref} \tag{12}$$

## References

Agliardi F, Scuderi MM, Fusi N, Collettini C (2020) Slow-to-fast transition of giant creeping rockslides modulated by undrained loading in basal shear zones. Nat Commun 11(1)

Blasio D, Vittorio F, Medici L (2017) Microscopic model of rock melting beneath landslides calibrated on the mineralogical analysis of the Köfels frictionite. Landslides 14(1):337–350

Bohloli B, Soldal M, Smith H, Skurtveit E, Choi JC, Sauvin G (2020) Frictional properties and seismogenic potential of caprock shales. Energies 13(23):6275

Bontemps N, Lacroix P, Larose E, Jara J, Taipe E (2020) Rain and small earthquakes maintain a slow-moving landslide in a persistent critical state. Nat Commun 11(1)

Cappa F, Scuderi MM, Collettini C, Guglielmi Y, Avouac JP (2019) Stabilization of fault slip by fluid injection in the laboratory and in situ. Sci Adv 5(3), eaau4065

Clariana P (2004) El sinclinori de Tor-Casamanya. Estudi estratigràfic i estructural, Nova cartografia geológica a escala 1:25000. Tech. rept. Horitzó 6:3–15. Rev Centre Recerca Cièn Terra

Corominas J, Moya J, Lloret A, Gili JA, Angeli MG, Pasuto A, Silvano S (2000) Measurement of landslide displacements using a wire extensometer. Eng Geol 55(3):149–166

Corominas J, Iglesias R, Aguasca A, Mallorqui J, Fabregas X, Batlle X, Gili J (2014) Comparing satellite based and ground based radar interferometry and field observations at the Canillo landslide (Pyrenees)

Euroconsult SA (2017) Auscultacions inclinomètriques, piezomètriques i extensomètriques al moviment de massa del Forn. Tech. rept. Ref. U-1586-A23

Ferri F, Toro G. Di, Hirose T, Shimamoto T (2010) Evidence of thermal pressurization in high-velocity friction experiments on smectite-rich gouges. Terra Nova. https://doi.org/10.1111/j.1365-3121.2010.00955.x

Ghuman BS, Lal R (1985) Thermal conductivity, thermal diffusivity, and thermal capacity of some Nigerian soils. Soil Sci 139(1):74–80

Gili JA, Moya J, Corominas J, Crosetto M, Monserrat O (2021) Past, present and future monitoring at the vallcebre landslide (Eastern Pyrenees, Spain). Appl Sci 11(571)

Goren L, Aharonov E (2007) Long runout landslides: the role of frictional heating and hydraulic diffusivity. Geophys Res Lett 34(7)

Goren L, Aharonov E, Anders MH (2010) The long runout of the heart mountain landslide: heating, pressurization, and carbonate decomposition. J Geophys Res 115(B10)

Gruntfest IJ (1963) Thermal Feedback in Liquid Flow; Plane Shear at Constant Stress. Transactions of the Society of Rheology 7(1):195–207

Hastings WK (1970) Monte Carlo sampling methods using Markov chains and their applications. Biometrika 57(1):97–109

Hicher PY (1974) Etude des proprietes mecaniques des argiles a l' aide d' essais triaxiaux, influence de la vitesse et de la temperature, Report of the soil mechanics laboratory,. Tech. rept. Ecole Central, de Paris

Hueckel T, François B, Laloui L (2009) Explaining thermal failure in saturated clays. Géotechnique 59(3):197–212

Intrieri E, Carlà T, Gigli G (2019) Forecasting the time of failure of landslides at slope-scale: a literature review. Earth Sci Rev 193:333–349

Lacroix P, Handwerger AL, Bièvre G (2020) Life and death of slow-moving landslides. Nat Rev Earth Environ 1(8):404–419

Leinenkugel H-J (1976) Deformations und festigkeitverhalten bindiger erdstoffe: experimental ergebnisse und ihre physikalische Deutung. Ph.D. thesis, Karlsruhe University, Karlsruhe, Germany

Lizárraga JJ, Buscarnera G (2020) Probabilistic modeling of shallow landslide initiation using regional scale random fields. Landslides 17(8):1979–1988
Madritsch H, Millen B (2007) Hydrogeologic evidence for a continuous basal shear zone within a deep-seated gravitational slope deformation (Eastern Alps, Tyrol, Austria). Landslides 4(05):149–162
Niemeijer A, Marone C, Elsworth D (2010) Frictional strength and strain weakening in simulated fault gouge: competition between geometrical weakening and chemical strengthening. J Geophys Res 115(B10)
Rattez H, Veveakis M (2020) Weak phases production and heat generation control fault friction during seismic slip. Nat Commun 11(1):350
Raychaudhuri S (2008) Introduction to Monte Carlo simulation. In: 2008 winter simulation conference. Miami, FL, USA: Winter Simulation Conference, pp 91–100
Rice JR (2006) Heating and weakening of faults during earthquake slip. J Geophys Res Solid Earth 111(B5)
Seguí C, Tauler E, Planas X, Moya J, Veveakis M (2020) The interplay between phyllosilicates fabric and mechanical response of deep-seated landslides. Landslides, Aug, The case of El Forn de Canillo landslide (Andorra)
Seguí C, Rattez H, Veveakis M (2020) On the stability of deep-seated landslides. The Cases of Vaiont (Italy) and Shuping (Three Gorges Dam, China). J Geophys Res Earth Surface, 125(7)
Song Z, Li X, Lizárraga JJ, Zhao L, Buscarnera G (2020) Spatially distributed landslide triggering analyses accounting for coupled infiltration and volume change. Landslides 17(12):2811–2824
Vardoulakis I (2002) Steady shear and thermal run-away in clayey gouges. Int J Solids Struct 39(13):3831–3844
Veveakis E, Alevizos S, Vardoulakis I (2010) Chemical reaction capping of thermal instabilities during shear of frictional faults. J Mech Phys Solids 58(9):1175–1194
Veveakis E, Vardoulakis I, Di Toro G (2007) Thermoporomechanics of creeping landslides: the 1963 Vaiont slide, northern Italy. J Geophys Res, 112(F3)
Zhao N, Zhang R, Yan E, He X, Liu J (2020) A dynamic model for rapid startup of high-speed landslides based on the mechanism of friction-induced thermal pressurization considering vaporization. Landslides 17(7):1545–1560

**Carolina Seguí**(✉)
RWTH Aachen University, Aachen, Germany
Email: segui@gut.rwth-aachen.de

**Manolis Veveakis**
Duke University, Durham, NC, USA
Email: manolis.veveakis@duke.edu